# PCM-Based Energy Storage Systems for Solar Water Heating


**Akshay Sharma, Prasenjit Rath, and Anirban Bhattacharya**

## 1 Introduction

In recent years, there has been a prominent shift toward the use of renewable energy sources instead of using fossil fuel for energy generation. Use of renewable energy sources has multiple benefits such as the reduction of greenhouse gas emission and long-term sustainability. Among different renewable energy sources, solar energy is the most widely available and has been considered for large-scale energy production. Although solar energy has lot of potential for electricity generation, one of the most widely used applications of solar energy is domestic water heating. In solar water heating, cold water is directly heated using incident solar radiation without the necessity of any external power source.

### *1.1 Solar Domestic Water Heating*

Solar domestic water heaters have been used for many decades due to their simplicity. A typical solar water heater consists of a solar energy collector which heats a heat transfer fluid or water directly. The heating is done by concentrating the incident solar radiation using reflector plates which focus the energy on a cylindrical channel carrying the heat transfer fluid. The hot fluid is then used for heating water stored in a storage tank. Depending on the design, the water in the storage tank can also be directly circulated through the collector and directly heated. Whenever, hot water is necessary for domestic applications, the hot water from the storage tank is provided.

A. Sharma · P. Rath · A. Bhattacharya (✉)
School of Mechanical Sciences, IIT Bhubaneswar, Bhubaneswar, Odisha 752050, India
e-mail: anirban@iitbbs.ac.in



H. Tyagi et al. (eds.), *New Research Directions in Solar Energy Technologies*,
Energy, Environment, and Sustainability,
https://doi.org/10.1007/978-981-16-0594-9_14

The main advantage of this type of water heating system is that it directly converts solar energy to thermal energy and thus has high efficiency of conversion. In comparison, an electric water heater will convert electricity to thermal energy and the electricity is previously obtained by conversion of thermal or chemical energy. Also, solar energy is widely available and thus can support the design and installation of small independent units for each user. However, installation of solar domestic heaters requires significant capital costs although the high initial cost is offset by the subsequent lower energy cost. The other major disadvantage of solar water heaters is that they can only provide hot water intermittently during daytime depending on weather conditions and cannot provide hot water during night. It is necessary to use an effective storage method to provide hot water as and when required and particularly during night time.

## *1.2 Energy Storage for Solar Water Heater*

There are two main ways to store energy for solar water heaters (Kee et al. 2018). The traditional designs use a storage tank which is well insulated and stores heated water for future use. The water in the storage tank can be directly heated by supplying it to the collector or it can be heated using a separate heat transfer fluid which transfers thermal energy as sensible heat to the stored water. Various designs have been proposed for the storage tank to increase its storage effectiveness. However, in spite of improved designs, the stored water loses the stored heat gradually and cannot retain it for long durations. This can be overcome by using a large storage tank with high thermal inertia. However, such a design will increase the weight of the system significantly and will require a more robust design for domestic roof top installation.

To limit the weight of the system, storage tanks incorporating phase change materials (PCM) have been developed (Kee et al. 2018; Seddegh et al. 2015; Abokersh et al. 2018). PCM store energy as latent heat by melting during the charging process. When energy is required to be extracted, the PCM is solidified and the stored latent energy is released. Since latent heat of melting is considerably higher as compared to sensible energy change for a substance, significantly lower mass of storage material is required for storing the same quantity of energy.

## *1.3 PCM-Based Solar Water Heater*

A number of designs for PCM-based solar water heaters have been proposed over the years due to the high energy storage density of PCM (Cabeza et al. 2002; Mehling et al. 2003; Al-Hinti et al. 2010; Oró et al. 2012; Kousksou et al. 2011; Fazilati and Alemrajabi 2013; Bouadila et al. 2014). Another advantage of using PCM is that the energy can be extracted at a constant temperature. Thus, a relatively constant temperature supply of hot water can be maintained for domestic applications. Also,

by incorporating multiple PCMs with different melting temperatures, water can be extracted at different temperatures for different applications.

For PCM-based solar water heaters, the PCM is either stored in separate chambers to avoid mixing with water (Al-Hinti et al. 2010; Kousksou et al. 2011; Prakash et al. 1985; Bansal and Buddhi 1992) or it is encapsulated in spherical shells which are placed in the storage tank (Nallusamy et al. 2007; Reddy et al. 2012). Melting takes place by supplying hot water from the solar collector which passes over the encapsulated PCM or in between the PCM chambers. For energy extraction, cold water is circulated around the PCM chambers or capsules which removes energy from the PCM and heats the water. The hot water is supplied for domestic applications. During this discharge process, the PCM converts back to the solid phase. For solar water heaters, the PCM undergoes repeated cycles of charging and discharging during which it melts and solidifies alternately. Low thermal conductivity of PCM restricts the total quantity of energy that can be stored in a limited time although the total storage capacity may be higher. Different methods have been proposed for increasing the effective thermal conductivity of PCM-based energy storage systems such as the use of metal fins (Zhang and Faghri 1996; Ismail et al. 2001; Nayak et al. 2006; Gharebaghi and Sezai 2007), metal or graphite foams (Zhou and Zhao 2011; Alshaer et al. 2015; Meng and Zhang 2017; Dinesh and Bhattacharya 2019, 2020; Joshi and Rathod 2019), nanoparticles (Shaikh et al. 2008; Fan and Khodadadi 2012; Sahoo et al. 2019), and encapsulated PCM (Hawlader et al. 2003; Fukahori et al. 2016).

One of the important aspects of designing a suitable PCM-based solar water heater is proper selection of PCM. The important properties that need to be considered for selection of PCM are as follows.

1. High latent heat of phase change which leads to large energy storage density.
2. Suitable temperature of melting and solidification so that heat transfer can occur at the desired temperature depending on the application.
3. Less shrinkage and expansion during solidification and melting.
4. High specific heat in both liquid and solid phases so that significant sensible energy storage can occur. However, this will lead to longer time for the system to reach melting temperature and may be detrimental if heat transfer is required at a specific temperature.
5. Relatively large thermal conductivity for higher heat transfer rates.
6. Chemical stability of PCM over large number of charging and discharging cycles.
7. Low cost and easy availability of PCM.
8. Non-corrosive and non-toxic nature for long-term safety of the system.

Among these properties the most important property for selection of PCM is high energy storage density and suitable temperature of melting and solidification depending on the requirement.

Another important aspect of PCM-based solar water heater is storage tank design. Among different types of storage tank designs one of the most popular is to use a shell and tube heat exchanger with a cylindrical storage tank and cylindrical pipes passing through the tank for carrying charging and discharging water (Nagano et al.

2004; Adine and Qarnia 2009; Hosseini et al. 2012; Mat et al. 2013; Mahfuz et al. 2014; Shrivastava and Chakraborty 2019). Typically, it consists of two concentric cylinders. The outer cylinder contains the PCM while the inner cylinder acts as the flow channel for charging and discharging. The aim of this chapter is to present a study on the effect of important parameters on the performance of shell- and tube-type PCM-based solar water heater. To do this, a two-channel energy storage system is considered with PCM in the outer chamber and water flowing through the inner channel. An enthalpy-porosity-based model is developed to simulate both melting and solidification of PCM. The model is capable of simulating flow of water during charging and discharging, heat transfer in the water, PCM and the separating aluminum wall, phase change and buoyancy driven natural convection in the PCM.

## 2 Problem Description

For the simulations, a two-dimensional problem domain is considered, as shown in Fig. 1. The problem domain consists of an inner channel through which water flows during charging and discharging. PCM is contained in the outer chamber. The two chambers are separated by a thin wall of aluminum. Only half of the system is considered for the simulations. It is assumed that the effect of natural convection is not strong enough to significantly alter the melting pattern of PCM at the top and bottom of the flow channel. Similar observations have been made in Morales-Ruiz et al. (2016). During charging, hot water enters the inner channel from the left side of the domain and exits from the right. During discharging, the flow direction is reversed and cold water enters from the right side.

It is assumed that the PCM is in solid phase initially. The temperature in the entire domain is uniform initially with a value less than the melting temperature of PCM. For the flow, velocity boundary conditions consist of specified uniform velocity at the inlet and outflow conditions on the opposite side of the flow channel. As mentioned previously, the flow direction changes depending on the charging or discharging process. All the other boundaries have zero velocity condition except the bottom boundary which has symmetry conditions. For the heat transfer, uniform

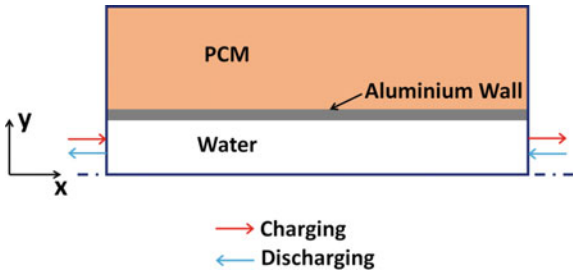


**Fig. 1** Schematic representation of the problem domain

temperature boundary condition is applied at the inlet of the flow channel. All the other boundaries are kept insulated.

## 3 Mathematical Model

The developed model consists of two coupled parts: The flow model and the phase change model. The flow model consists of the continuity and momentum equations which are formulated using volume averaging of the two phases. It should be noted here that the two-phase model is only required for the PCM domain. For calculating the flow in the water channel, only liquid phase momentum equations are considered as described later in Sect. 3.2. However, the numerical code for implementing the flow equations is developed in a generalized form with the capability of solving for both solid and liquid phases. Depending on the conditions, the model appropriately reduces to single phase liquid, single phase solid, or two-phase form. The phase change model is developed using the enthalpy-porosity technique (Voller et al. 1989; Chakraborty and Dutta 2001) which requires the solution of the enthalpy-based energy conservation equation.

All the governing equations are formulated and solved in non-dimensional form. Although for the PCM, water channel, and solid metal wall, the governing equations are different as given in Sects. 3.1, 3.2 and 3.3, the equations are implemented in the CFD code in a generalized form where a single formulation is sufficient to describe the governing equations for all the regions. Depending on different material parameters, the equations reduce to the appropriate equations for the PCM, water and solid metal regions while solving. Hence, the non-dimensionalization of the governing equations for all the three regions is done in the same way by using the same set of parameters. The non-dimensional parameters are taken as $x^* = x/L$, $y^* = y/L$, $T^* = (T - T_{\min})/(T_{\max} - T_{\min})$, $u^* = uL/\alpha_{\text{pcm}}$, $v^* = vL/\alpha_{\text{pcm}}$, $t^* = t\alpha_{\text{pcm}}/L^2$, $\rho^* = \rho/\rho_{\text{pcm}}$, $K^* = K/K_{\text{pcm}}$, $C^* = C/C_{\text{avg}}$, $(\rho C)^* = \rho C/(\rho C)_{\text{avg}}$, $\alpha_{\text{pcm}} = K_{\text{pcm}}/(\rho_{\text{pcm}} C_{\text{avg}})$. $x$ and $y$ denote the distance along the two coordinate axes, $L$ is the length of the domain, $T$ is the temperature and $T_{\min}$ and $T_{\max}$ are the minimum and maximum temperatures equal to the cold water temperature and hot water temperature, respectively. $u$ and $v$ are the velocity components along the $x$ and $y$ directions, $\alpha$ is the thermal diffusivity, $t$ denotes time, and $\rho$ denotes density. $K$ and $C$ are the thermal conductivity and specific heat, respectively. The subscripts 'pcm' and 'avg' denote the properties of PCM and average of two phases, respectively. The non-dimensional values are represented by the superscript '*'. The governing equations assume different forms for the three regions: PCM, water, and metal wall as described in the following sections.

### 3.1 PCM Volume

For the PCM, both flow and energy conservation equations need to be solved. The flow equations need to be solved as the effect of natural convection is considered in the model. To solve for flow in the domain, the following continuity and momentum equations are required.

$$\frac{\partial \rho^*}{\partial t^*} + \frac{\partial (\rho^* u^*)}{\partial x^*} + \frac{\partial (\rho^* v^*)}{\partial y^*} = 0 \tag{1}$$

$$\rho^*_{\text{pcm}}\left[\frac{\partial u^*}{\partial t^*} + u^*\frac{\partial u^*}{\partial x^*} + v^*\frac{\partial u^*}{\partial y^*}\right] = -\frac{\partial p^*}{\partial x^*} + \text{Pr}\left[\frac{\partial^2 u^*}{\partial x^{*2}} + \frac{\partial^2 u^*}{\partial y^{*2}}\right] + Au^* \tag{2}$$

$$\rho^*_{\text{pcm}}\left[\frac{\partial v^*}{\partial t^*} + u^*\frac{\partial v^*}{\partial x^*} + v^*\frac{\partial v^*}{\partial y^*}\right] = -\frac{\partial p^*}{\partial y^*} + \text{Pr}\left[\frac{\partial^2 v^*}{\partial x^{*2}} + \frac{\partial^2 v^*}{\partial y^{*2}}\right] + Av^* + \text{Pr}\,.\text{Ra}\left(T^* - T^*_m\right) \tag{3}$$

In Eqs. (1–3), Pr and Ra denote the Prandtl number and Rayleigh number. Prandtl number is defined as $\text{Pr} = \mu_{\text{pcm}} \Big/ \rho_{\text{pcm}}\alpha_{\text{pcm}}$ while Rayleigh number is defined as $\text{Ra} = \rho_{\text{pcm}} g \beta_{\text{pcm}} L^3 (T_{\max} - T_{\min}) \Big/ \mu_{\text{pcm}}\alpha_{\text{pcm}}$ where $\beta_{\text{pcm}}$ is the coefficient of volume expansion of PCM and $g$ is the acceleration due to gravity. The term $\text{Pr}\,.\text{Ra}\left(T^* - T^*_m\right)$ represents the effect of natural buoyancy.

The presence of solid phase is incorporated through the terms $Au^*$ and $Av^*$. $A$ is defined as $A = C(1-\varepsilon)^2 \big/ \varepsilon^3 + b$ where $\varepsilon$ is the liquid fraction. $C$ is taken as a very large valued constant and $b$ is a small number required to avoid division by zero in the numerical solution. These two terms approximate the increased resistance for flow in the two-phase region and drive the velocity to zero in the solid phase.

The phase change and heat transfer in the PCM are modeled using the following volume averaged energy equation.

$$\rho^*_{\text{pcm}} C^*_L\left[\frac{\partial T^*}{\partial t^*} + u^*\frac{\partial T^*}{\partial x^*} + v^*\frac{\partial T^*}{\partial y^*}\right] = K^*_{\text{pcm}}\left[\frac{\partial^2 T^*}{\partial x^{*2}} + \frac{\partial^2 T^*}{\partial y^{*2}}\right] + S_{h1} + S_{h2} \tag{4}$$

In Eq. (4), $S_{h1}$ is a source term which represents the effect of latent heat of phase change. $S_{h1}$ is defined as $S_{h1} = -\frac{1}{\text{Ste}}\left[\rho^*_{\text{pcm}}\frac{\partial \varepsilon}{\partial t^*} - \nabla\left(\rho^*_{\text{pcm}}\vec{u}^*\varepsilon\right)\right]$ where Ste is the Stefan number. The Stefan number is defined as $\text{Ste} = C_{\text{avg}}(T_{\max} - T_{\min}) \big/ L_f$ where $L_f$ is the latent heat of phase change. The second source term, $S_{h2}$, can be written as $S_{h2} = -\rho^*_{\text{pcm}}\left[\left(C^*_{\text{avg}} - C^*_L\right)\frac{\partial T^*}{\partial t} + T^*\frac{\partial C^*_{\text{avg}}}{\partial t}\right] - \frac{\rho^*_{\text{pcm}} T_{\min}}{(T_{\max} - T_{\min})}\frac{\partial C^*_{\text{avg}}}{\partial t}$ and arises due to the modification of the volume averaged equation in the given form.

### 3.2 Water Channel

For the water channel, the continuity and momentum equations are formulated as follows.

$$\frac{\partial \rho^*_{\text{water}}}{\partial t^*} + \frac{\partial \left(\rho^*_{\text{water}} u^*\right)}{\partial x^*} + \frac{\partial \left(\rho^*_{\text{water}} v^*\right)}{\partial y^*} = 0 \tag{5}$$

$$\rho^*_{\text{water}}\left[\frac{\partial u^*}{\partial t^*} + u^*\frac{\partial u^*}{\partial x^*} + v^*\frac{\partial u^*}{\partial y^*}\right] = -\frac{\partial p^*}{\partial x^*} + \text{Pr}\,\frac{\mu_{\text{water}}}{\mu_{\text{pcm}}}\left[\frac{\partial^2 u^*}{\partial x^{*2}} + \frac{\partial^2 u^*}{\partial y^{*2}}\right] \tag{6}$$

$$\rho^*_{\text{water}}\left[\frac{\partial v^*}{\partial t^*} + u^*\frac{\partial v^*}{\partial x^*} + v^*\frac{\partial v^*}{\partial y^*}\right] = -\frac{\partial p^*}{\partial y^*} + \text{Pr}\,\frac{\mu_{\text{water}}}{\mu_{\text{pcm}}}\left[\frac{\partial^2 v^*}{\partial x^{*2}} + \frac{\partial^2 v^*}{\partial y^{*2}}\right] \tag{7}$$

As the entire water channel contains only liquid water, the flow resistance source terms to represent solid phase are not present in Eqs. (6 and 7). Natural buoyancy effects are also not considered for the water flow as the velocity due to forced flow is drastically higher in this case.

The heat transfer in the water is governed by the following energy conservation equation.

$$\rho^*_{\text{water}} C^*_{\text{water}}\left[\frac{\partial T^*}{\partial t^*} + u^*\frac{\partial T^*}{\partial x^*} + v^*\frac{\partial T^*}{\partial y^*}\right] = K^*_{\text{water}}\left[\frac{\partial^2 T^*}{\partial x^{*2}} + \frac{\partial^2 T^*}{\partial y^{*2}}\right] \tag{8}$$

### 3.3 Solid Metal Wall

For the metal wall separating the PCM from the heat transfer fluid, only the energy transfer needs to be considered. The temperature evolution in this region is governed by the following energy equation.

$$\rho^*_{\text{Solid}} C^*_{\text{Solid}}\left(\frac{\partial T^*}{\partial t^*}\right) = K^*_{\text{Solid}}\left[\frac{\partial^2 T^*}{\partial x^{*2}} + \frac{\partial^2 T^*}{\partial y^{*2}}\right] \tag{9}$$

In Eqs. (5–9), the subscripts 'water' and 'solid' denote the water and solid metal regions, respectively.

## 4 Numerical Solution

The governing equations are discretized in a Cartesian coordinate framework using a finite volume approach. For solving the equations, the SIMPLER algorithm given in

Patankar (2018) is employed. The convection–diffusion terms are discretized using the power law scheme. The discretized equations are solved using line-by-line tri-diagonal matrix algorithm (TDMA) with multiple sweeping from all possible directions. The numerical model is implemented using an in-house code developed using Fortran 90. The developed code is based on the previous numerical program described in Sahoo et al. (2016). It has been validated with analytical solution for phase change and with experimental results for melting of PCM in Sahoo et al. (2016). The solution algorithm consists of the following steps.

1. At first the domain is defined and the numerical grid is generated.
2. The initial and boundary conditions are specified for the entire domain.
3. The liquid fraction values are set equal to zero for the PCM and metal and equal to one for the water. All the other properties are defined for all the regions.
4. The different source terms are calculated.
5. The flow field is calculated by solving the continuity and momentum equations.
6. The energy equation is solved for each region to obtain the temperature field.
7. The liquid fraction is calculated using the enthalpy update scheme given in Sahoo et al. (2016).
8. The solution is checked for convergence. If the solution has not converged, steps 4–7 are repeated until convergence is achieved.
9. The current values are stored for use in the next time step.
10. The calculation for the next time is started and the steps 4–9 are repeated until the time reaches the end of charging phase.
11. The discharging phase is started and the steps 4–9 are repeated until the end of simulation.

## 5 Results for a Single Charging and Discharging Cycle

### *5.1 Simulation Parameters*

All the simulations considered in this chapter consist of a single charging–discharging cycle. It is assumed that initially the PCM is in solid state kept at a low temperature. High-temperature water is passed through the inner channel which transfers heat to the PCM through the metal wall. At first, sensible heating of PCM occurs until it reaches the melting temperature. Subsequently, the PCM starts melting which continues until the entire PCM gets melted or the charging end time is reached. This is followed by the discharging cycle in which water at low temperature is passed through the channel from the opposite direction. Energy stored in the PCM is transferred to the water through the metal wall. The water goes out of the channel at a relatively high temperature. The PCM loses energy and solidifies back by latent heat removal. After complete solidification, the PCM supplies energy by losing sensible heat and thus undergoing reduction in temperature. This continues until the discharging cycle is stopped. For all the simulations presented in this chapter, paraffin wax is taken as

**Table 1** Thermophysical properties used for the simulations

| Property | Paraffin | Water | Aluminum |
|---|---|---|---|
| Latent heat (kJ/kg) | 169 | – | – |
| Thermal conductivity (W/m K) | 0.2 | 0.591 | 205 |
| Specific heat (J/kg K) | 2100 | 4187 | 910 |
| Density (kg/m$^3$) | 880 | 1000 | 2830 |
| Viscosity (Ns/m$^2$) | 0.007 | 0.001 | – |
| Melting temperature (°C) | 60–64 | – | – |
| Thermal expansion coefficient (K$^{-1}$) | 0.001 | – | – |

the PCM and the metal wall is assumed to be made of aluminum. The thermophysical properties of the different materials are specified in Table 1.

## *5.2 Simulation Prediction for a Single Charging and Discharging Cycle*

At first a single charging cycle for 20,000 s is considered which is immediately followed by a discharging cycle for 10,000 s. The initial temperature for the entire domain is taken as 20 °C. During the charging cycle, hot water enters the flow channel with a temperature of 80 °C and a velocity of 0.002 m/s. During the discharging cycle, cold water enters the flow channel with a temperature of 20 °C and a velocity of 0.001 m/s. The length of the channel is taken as 0.5 m. The thickness of the water channel (for the half domain as specified in the problem due to its symmetric nature) is taken as 3 cm, the thickness of the metal plate is 3 mm while that of the PCM region is 4 cm.

The evolution of temperature and liquid fraction contours is presented in Figs. 2 and 3. It is seen that initially the temperature rises quickly in the PCM and metal due to sensible heating. Subsequently, the rate of increase of temperature slows down as the energy is absorbed as latent heat due to melting of PCM. From the liquid fraction contours, it is observed that melting starts quickly over the entire metal plate initially. The rate of melting is highest near the inlet section of water. During the discharging cycle, the temperature of PCM near the metal wall decreases quickly and the PCM solidifies. PCM present at larger distances from the metal wall takes considerably higher time to solidify and maintains high temperature for a longer duration. The average temperature of water at the outlet is higher than that at the inlet.

To quantify the melting rate of PCM and temperature of water, the variation of liquid fraction of PCM during the entire charging–discharging cycle and the variation of outlet water temperature with time during charging and during discharging are shown in Fig. 4. It is seen that at the end of the charging cycle the liquid fraction of PCM is about 0.6 and it almost reaches 0 at the end of the discharge cycle. During

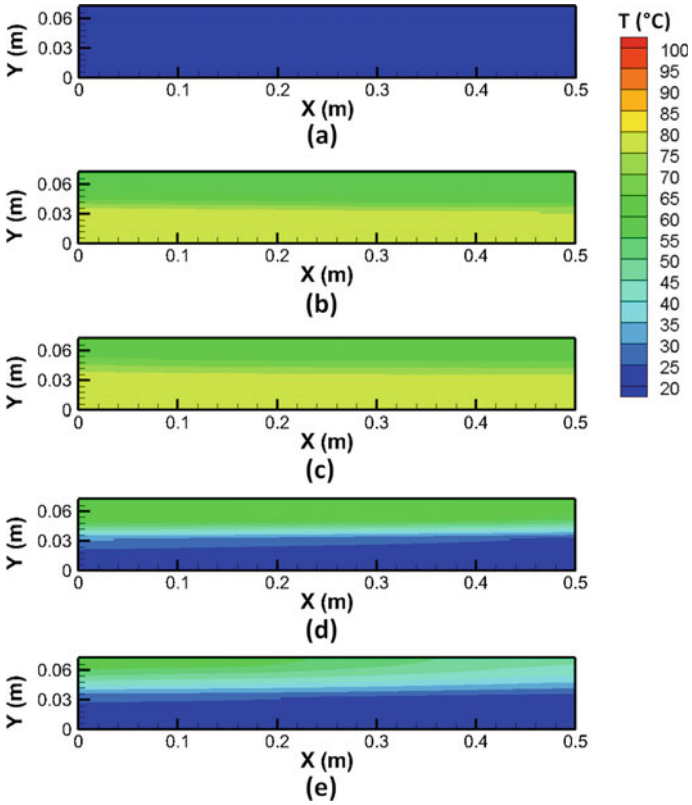


**Fig. 2** Temperature field at time. **a** 0 s, **b** 10,000 s, **c** 20,000 s, **d** 25,000 s, **e** 30,000 s

the charging cycle, the water outlet temperature is very low initially as most of its energy is transferred to the PCM due to the large temperature difference with the PCM. Another reason for the initial low outlet temperature is that the water channel is initially kept at 20 °C. However, the outlet temperature quickly increases which signifies that the rate of heat transfer to the PCM decreases. The outlet temperature remains slightly below 80 °C which results in reduced heat transfer to the PCM. During the discharge cycle, the average water temperature reaches a value of 31 °C but gradually drops to around 22.5 °C at the end of the discharge cycle.

## 6 Effect of Design Parameters

In this section, the effect of important design parameters such as the inlet flow conditions, the charging time, and the dimensions of the system are studied. Seven different parameters are considered: inlet temperature of water during charging, flow

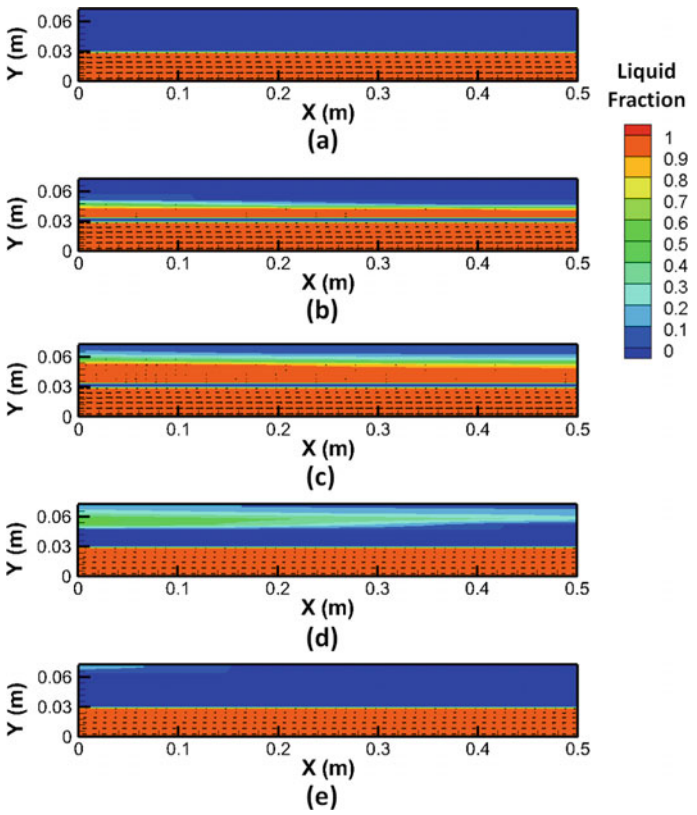


**Fig. 3** Liquid fraction and velocity vectors at time. **a** 0 s, **b** 10,000 s, **c** 20,000 s, **d** 25,000 s, **e** 30,000 s

velocity of water during charging, flow velocity of water during discharging, charging duration, length of the domain, width of the flow channel, and width of the PCM region. For each case, the values of all the parameters except the chosen parameter are kept constant and equal to that given in Sect. 5.2. For each study, the rate of melting and the temperature variation is compared.

## *6.1 Effect of Inlet Temperature of Water During Charging*

At first the effect of water inlet temperature is studied. Three cases are considered with inlet temperatures of 70 °C, 80 °C, and 90 °C. Charging is continued for 20,000 s which is followed by discharging for 10,000 s. Figures 5 and 6 present the comparison of temperature and liquid fraction for the three cases after the end of the charging cycle. It can be observed that the increase in temperature is very less for the 70 °C

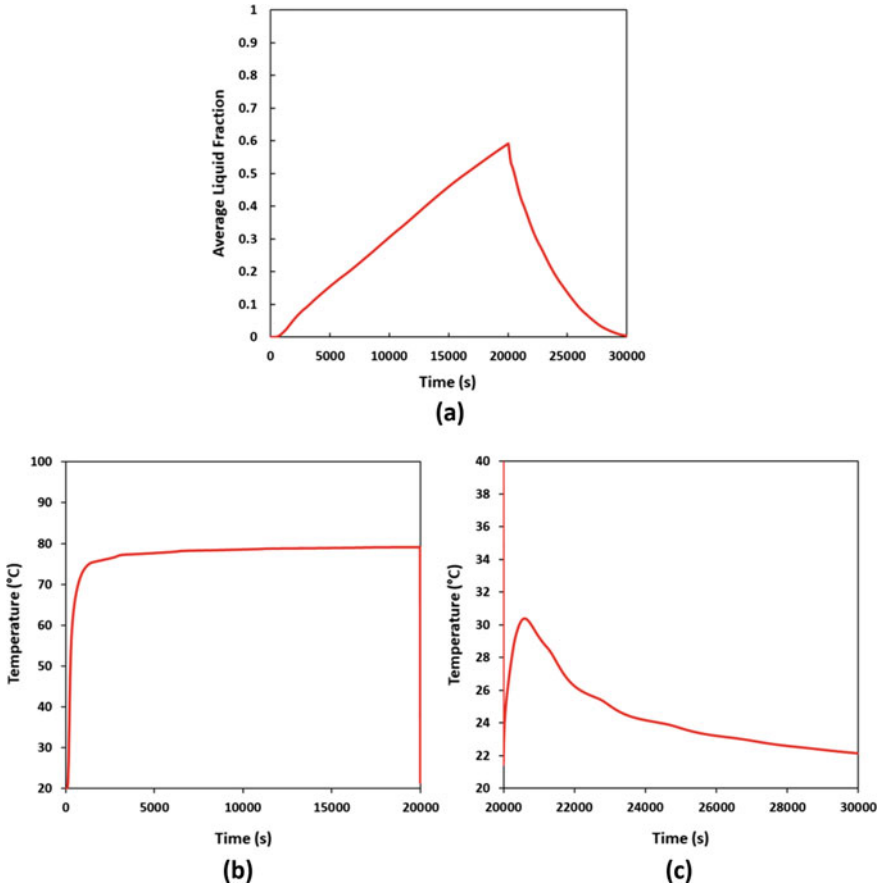


**Fig. 4** Variation of **a** liquid fraction with time during the entire cycle, **b** water outlet temperature during charging, and **c** water outlet temperature during discharging

case and the corresponding melting is also small. On the other hand, for high inlet temperature, the rate of melting is significantly higher. The temperature of the PCM near the wall also shows a similar trend although the temperature of PCM far away from the wall is relatively similar because of the effect of phase change between this region and the water.

Figure 7 presents a quantitative comparison of melting and temperature evolution for the three cases. From Fig. 7a, it is observed that the liquid fraction is significantly higher both during the charging and discharging cycles for higher inlet temperature. The water outlet temperature (Fig. 7b) during charging shows similar trends for all the cases as described previously in Sect. 5.2. The water outlet temperature during the discharge is improved significantly for the two high-temperature cases (Fig. 7c). As the water outlet temperature during discharge is the most important parameter for domestic heating applications, the time durations for which water is obtained at

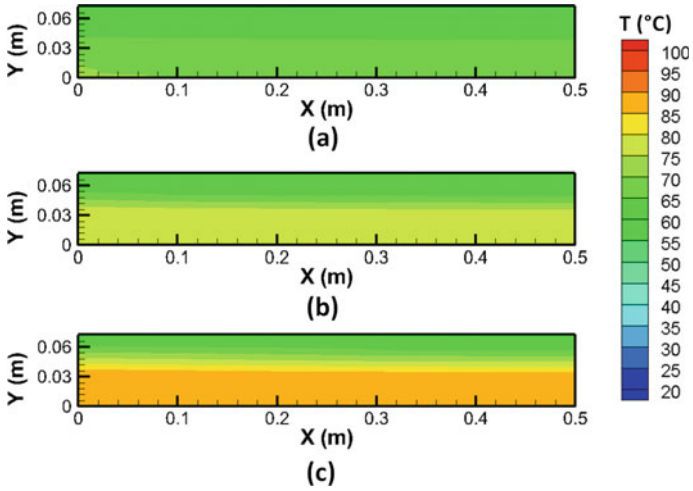


**Fig. 5** Temperature field at the end of charging cycle ($t = 20{,}000$ s) with water inlet temperature of **a** 70 °C, **b** 80 °C, **c** 90 °C

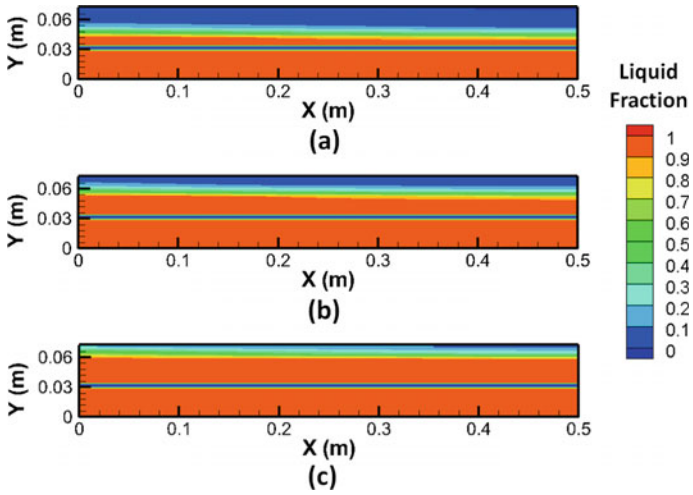


**Fig. 6** Liquid fraction at the end of charging cycle ($t = 20{,}000$ s) with water inlet temperature of **a** 70 °C, **b** 80 °C, **c** 90 °C

temperatures above 30 °C and 25 °C are compared in Fig. 7d. It is seen that water at more than 30 °C is obtained from the high-temperature system for about 650 s while the low-temperature system cannot provide water at this temperature threshold. For the high-temperature case, water temperature during the discharge is above 25 °C for about 3300 s which is considerably higher than that for the low-temperature case.

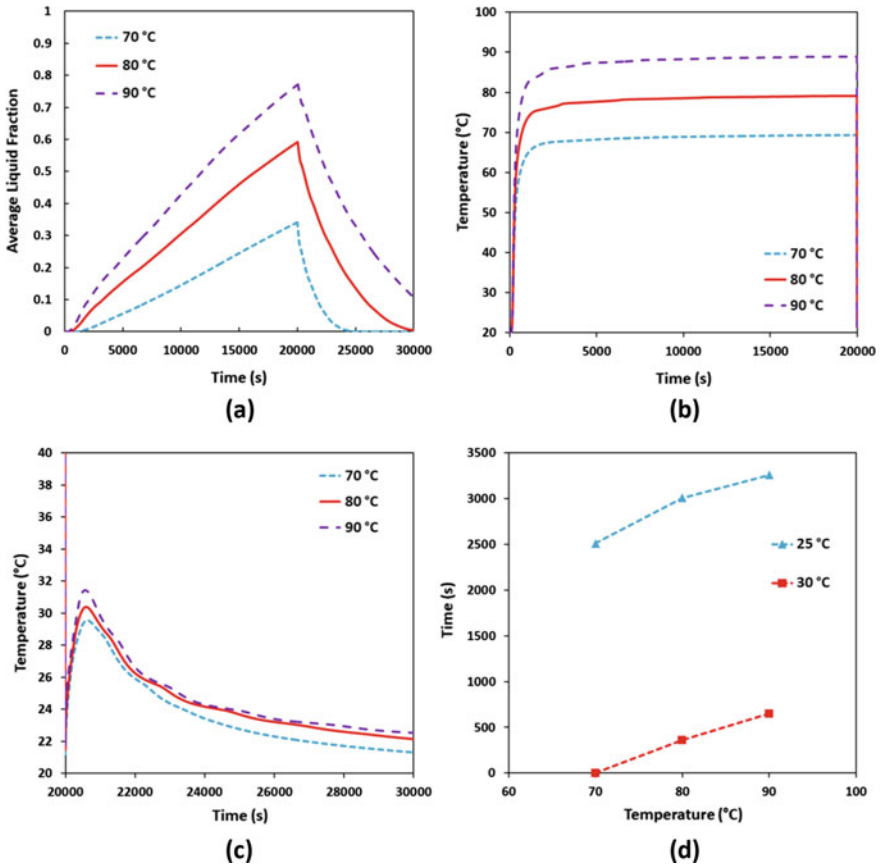


**Fig. 7** Variation of **a** liquid fraction with time, **b** water outlet temperature during charging, **c** water outlet temperature during discharging, **d** time for obtaining water at specified temperature

## *6.2 Effect of Inlet Flow Velocity During Charging*

In this section, the effect of inlet flow velocity during the charging process is considered. Three different inlet velocities are considered: 0.001 m/s, 0.002 m/s, and 0.004 m/s. Figures 8 and 9 present the comparison of temperature and liquid fraction for the three cases after the end of the charging cycle. Although not much difference can be seen from the temperature and liquid fraction contours, careful observation shows that the liquid fraction increases with increase in flow rate. This can be confirmed from Fig. 10a which shows that the rate of melting increases slightly with increase in flow velocity. However, the variation is not as significant as that seen with different inlet flow temperatures. The temperature variation during charging (Fig. 10b) shows that the rate of temperature increase is slightly higher for the high flow rate case initially although subsequently it becomes almost equal for all the

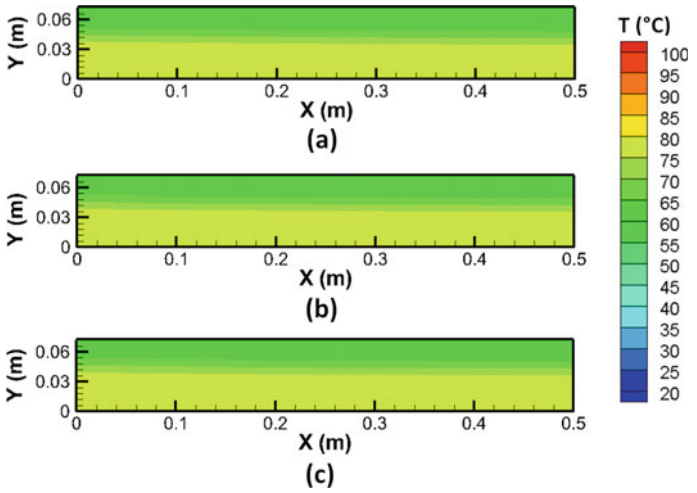


**Fig. 8** Temperature field at the end of charging cycle ($t$ = 20,000 s) with inlet flow velocity of **a** 0.001 m/s, **b** 0.002 m/s, and **c** 0.004 m/s

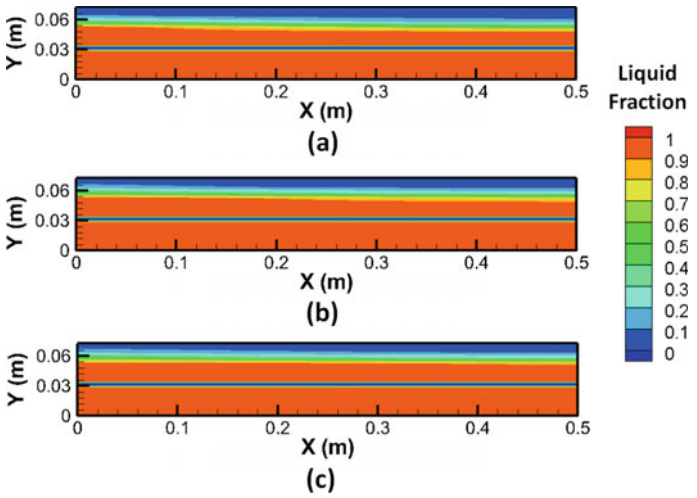


**Fig. 9** Liquid fraction at the end of charging cycle ($t$ = 20,000 s) with inlet flow velocity of **a** 0.001 m/s, **b** 0.002 m/s, and **c** 0.004 m/s

cases. The rate of temperature variation for all the three cases is similar during the discharging period (Fig. 10c). This is also confirmed from Fig. 10d which shows that the availability of water at a particular temperature is similar for all the cases considered. This study shows that the inlet flow velocity is not as important as the inlet flow temperature for improving the performance of PCM-based energy storage systems of this type.

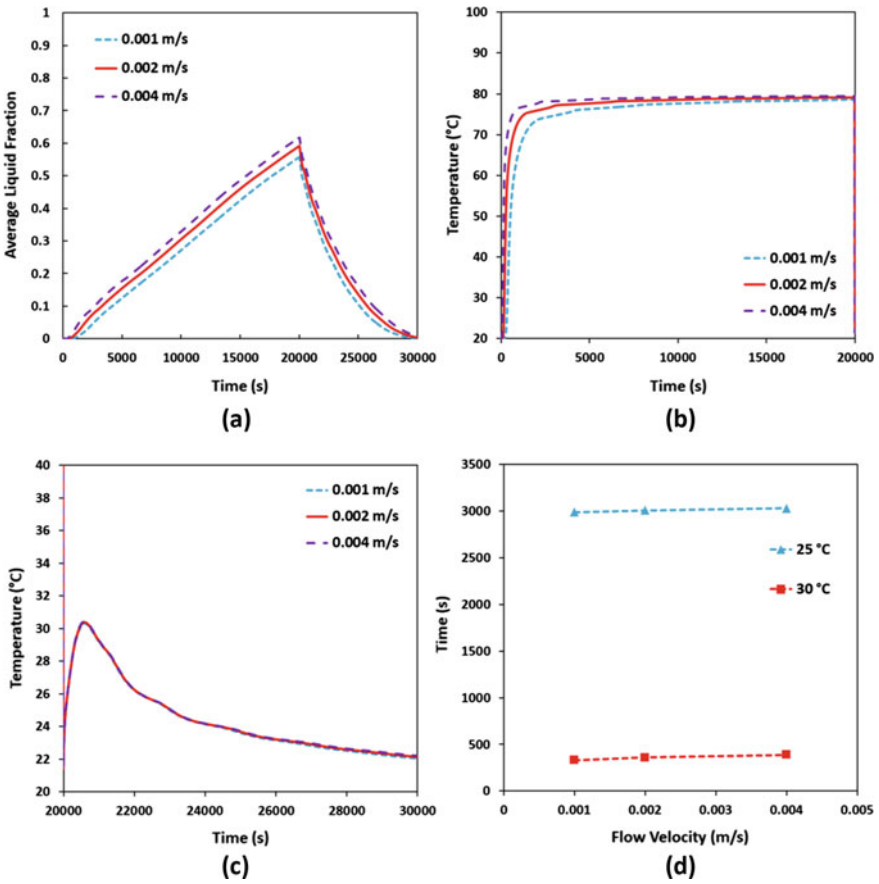


**Fig. 10** Variation of **a** liquid fraction with time, **b** water outlet temperature during charging, **c** water outlet temperature during discharging, and **d** time for obtaining water at specified temperature

## *6.3 Effect of Inlet Flow Velocity During Discharging*

The effect of discharge velocity is studied in this Sect. 3 different cases are considered with discharge flow velocity of 0.001 m/s, 0.002 m/s and 0.004 m/s. For all the 3 cases charging is done with hot water at 80 °C with a flow velocity of 0.002 m/s for 20,000 s. Subsequently, the discharging cycle takes place for 10,000 s. As the charging cycles are exactly similar for all the cases, the temperature distributions and liquid fraction distributions after charging are similar to that shown in Figs. 2 and 3. The temperature variation after the discharging cycle is shown in Fig. 11. It is seen that the temperature variation is almost similar in all the three cases. The variation of liquid fraction and temperature are analyzed in Fig. 12. Figure 12a shows that the rate of solidification is slightly higher for the high flow rate case. As discussed previously, the temperature during the charging cycle is exactly similar (Fig. 12b).

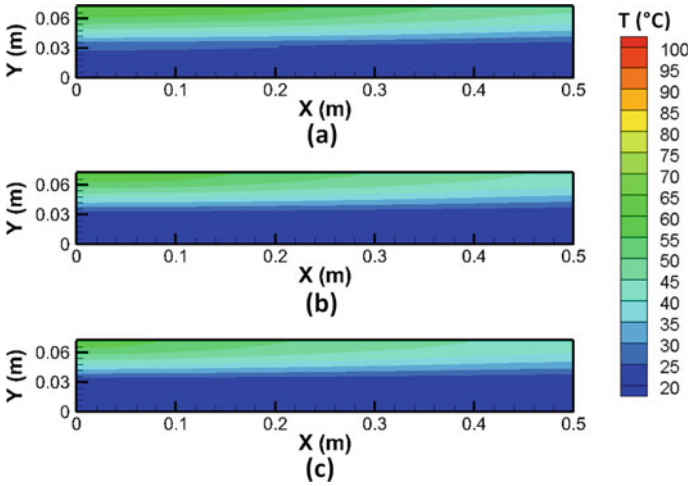


**Fig. 11** Temperature field at the end of discharging cycle ($t = 30{,}000$ s) with inlet flow velocity of **a** 0.001 m/s, **b** 0.002 m/s, and **c** 0.004 m/s

However, during the discharge cycle, lower flow rate results in significantly higher temperature for the entire discharge duration (Fig. 12c). Figure 12d shows that at higher flow rates, the outlet temperature is always less than 30 °C and the duration for which water is available at more than 25 °C is drastically reduced. If the results are compared with the predictions presented in Sect. 6.2, it can be observed that the discharge flow velocity has considerably larger effect on the available water temperature and thus is more important.

## *6.4 Effect of Charging Time*

Another important parameter which affects the charging process is the total duration of charging. Different charging times result in different quantities of energy stored and different temperature distribution after charging and thus affect the discharging process. For this analysis, three different charging times are considered: 10,000 s, 20,000 s and 30,000 s. The temperature and liquid fraction contours for the three cases after charging are compared in Figs. 13 and 14. It can be observed that although there is not much temperature variation due to the phase change process, the extent of melting is significantly higher after 30,000 s. This is clearly seen from Fig. 15a which shows that the liquid fraction is about 80% after 30,000 s and about 30% after 10,000 s. As a result, the entire PCM quickly solidifies during the discharging process for the 10,000 s case. On the other hand, large quantity of PCM remains in molten state even after the discharge cycle is complete for the 30,000 s case. The outlet water temperature during charging and discharging are presented in Fig. 15b,

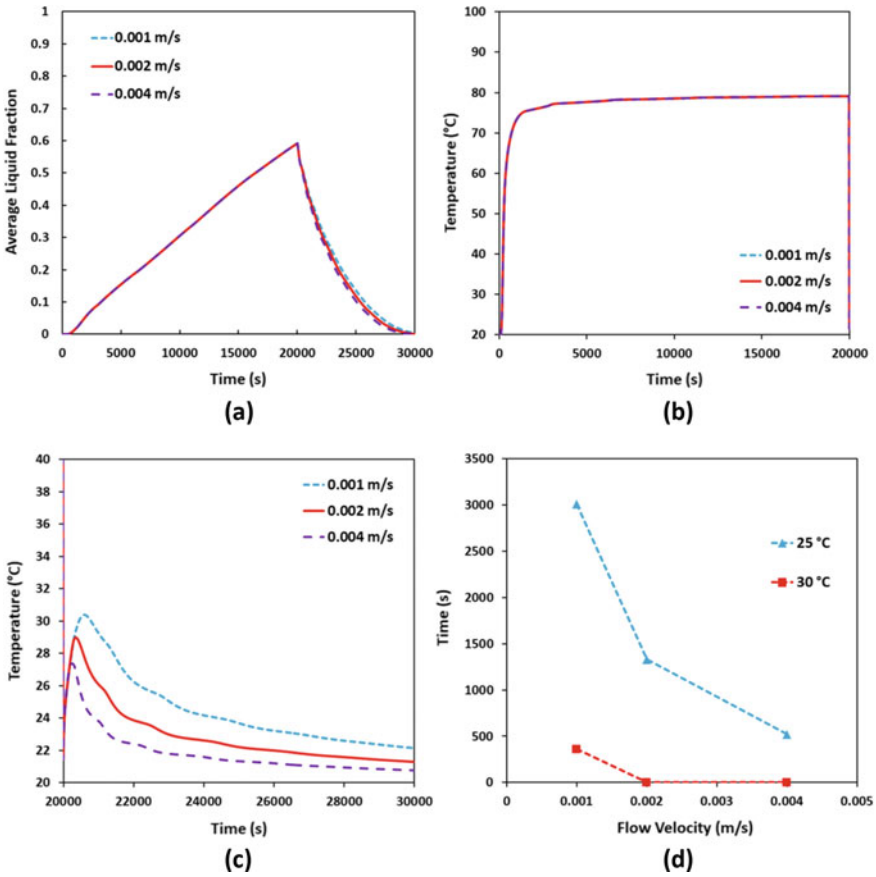


**Fig. 12** Variation of **a** liquid fraction with time, **b** water outlet temperature during charging, **c** water outlet temperature during discharging, and **d** time for obtaining water at specified temperature

c. It is seen that for the discharge cycle, the water outlet temperatures are similar for the 20,000 s and 30,000 s cases. For the low charging time case, the water outlet temperature is considerably lower. Figure 15d shows that the effect of charging time is more than that of charging flow velocity but less than that of charging temperature and discharging flow velocity.

## *6.5 Effect of Domain Length*

The effect of flow channel length is analyzed in this section. Three different domain lengths are considered: 0.25 m, 0.5 m, and 1.0 m. The temperature and liquid fraction contours for the three cases are compared in Figs. 16 and 17. It should be noted that

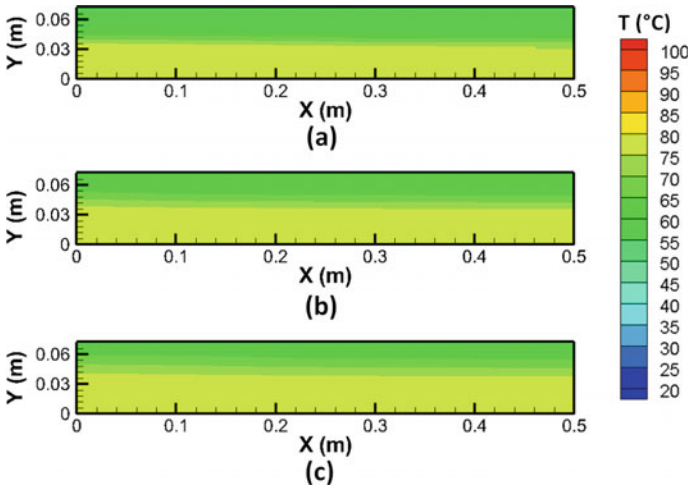


**Fig. 13** Temperature field at **a** $t = 10{,}000$ s, **b** $t = 20{,}000$ s, and **c** $t = 30{,}000$ s

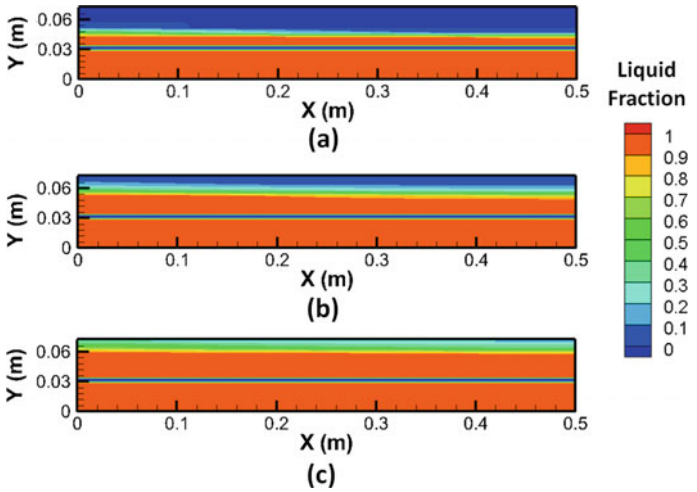


**Fig. 14** Liquid fraction variation at **a** $t = 10{,}000$ s, **b** $t = 20{,}000$ s, and **c** $t = 30{,}000$ s

all the three cases are shown by scaling them to the same length which changes the plotted width of the domain accordingly. It is seen that there is not much difference in temperature and melting rate for the three cases. Figure 18a, b shows that the liquid fraction and outlet temperature are slightly higher for the smaller domain. For smaller domain length, the reduction of water temperature is less during the charging cycle as the time of heat transfer to the PCM is less. As a result, the average liquid fraction is higher. However, because the lengths are different, the actual quantity of PCM melted is considerably higher for the longer domains. Figure 18c, d shows that

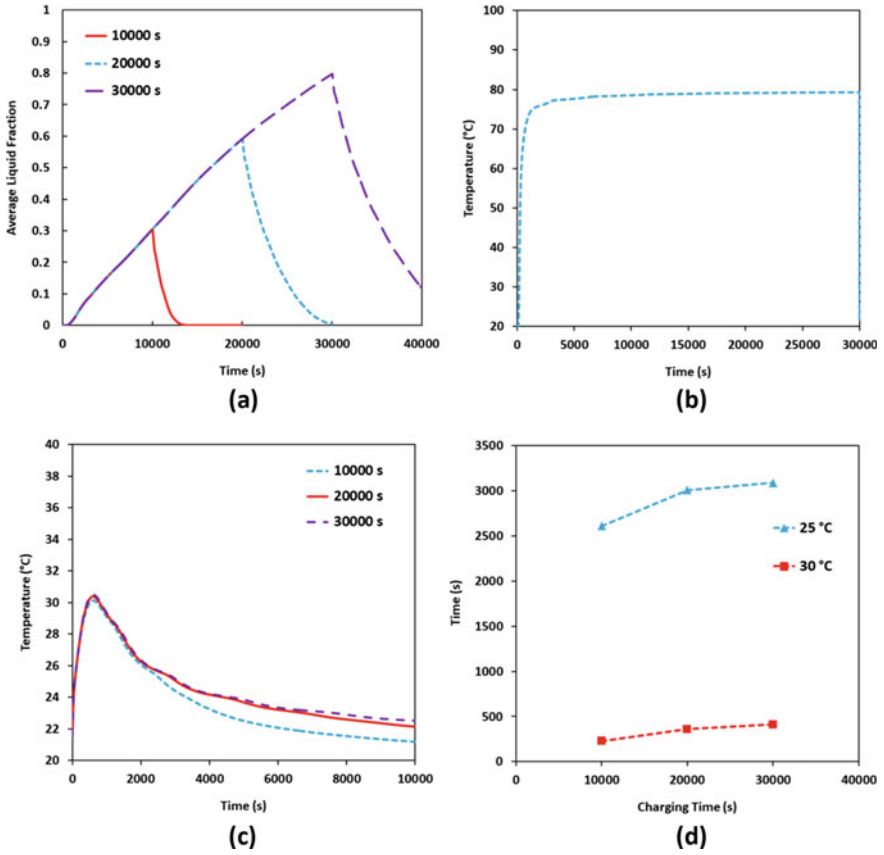


**Fig. 15** Variation of **a** liquid fraction with time, **b** water outlet temperature during charging, **c** water outlet temperature during discharging, and **d** time for obtaining water at specified temperature

the water outlet characteristics are drastically improved for longer domain sizes. It is seen that the domain length is the most important factor governing the discharge flow temperature.

## *6.6 Effect of Height of Flow Channel*

The effect of flow channel height is analyzed in this Sect. 3 and different channel heights are considered: 0.015 m, 0.03 m, and 0.06 m. The channel length is equal to 0.5 m for all the three cases. The inlet flow velocities are also kept constant and equal to 0.002 m/s during the charging process and 0.001 m/s during the discharging process. Figures 19 and 20 show the temperature and liquid fraction contours after

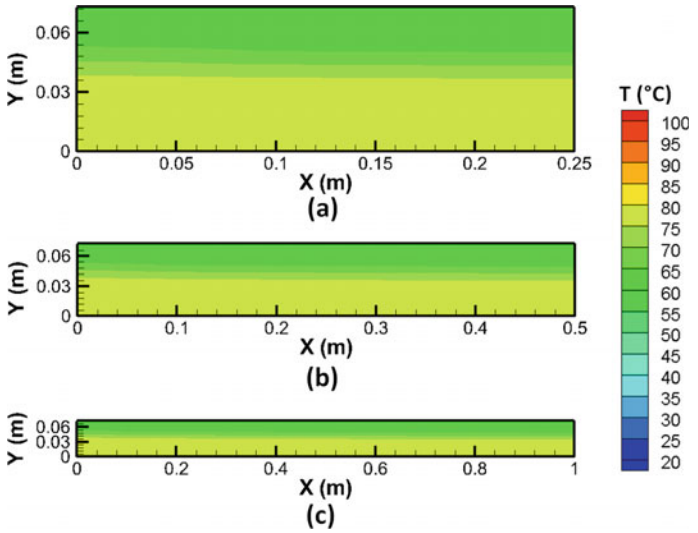


**Fig. 16** Temperature field at the end of charging cycle ($t = 20{,}000$ s) with domain length equal to **a** 0.25 m, **b** 0.5 m, and **c** 1.0 m

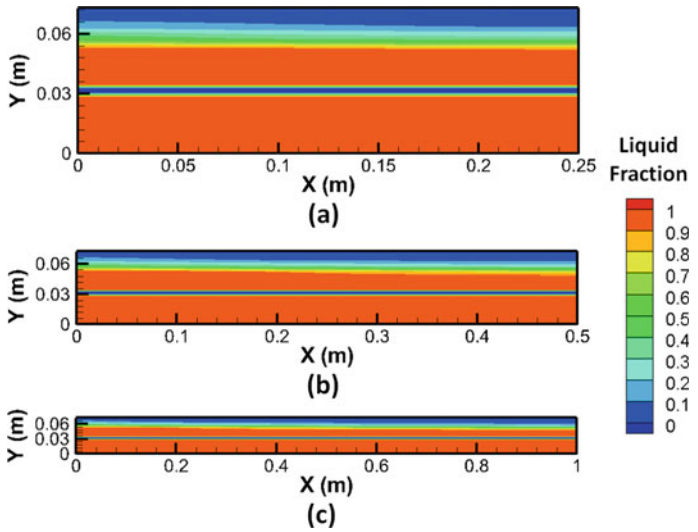


**Fig. 17** Liquid fraction at the end of charging cycle ($t = 20{,}000$ s) with domain length equal to **a** 0.25 m, **b** 0.5 m, and **c** 1.0 m

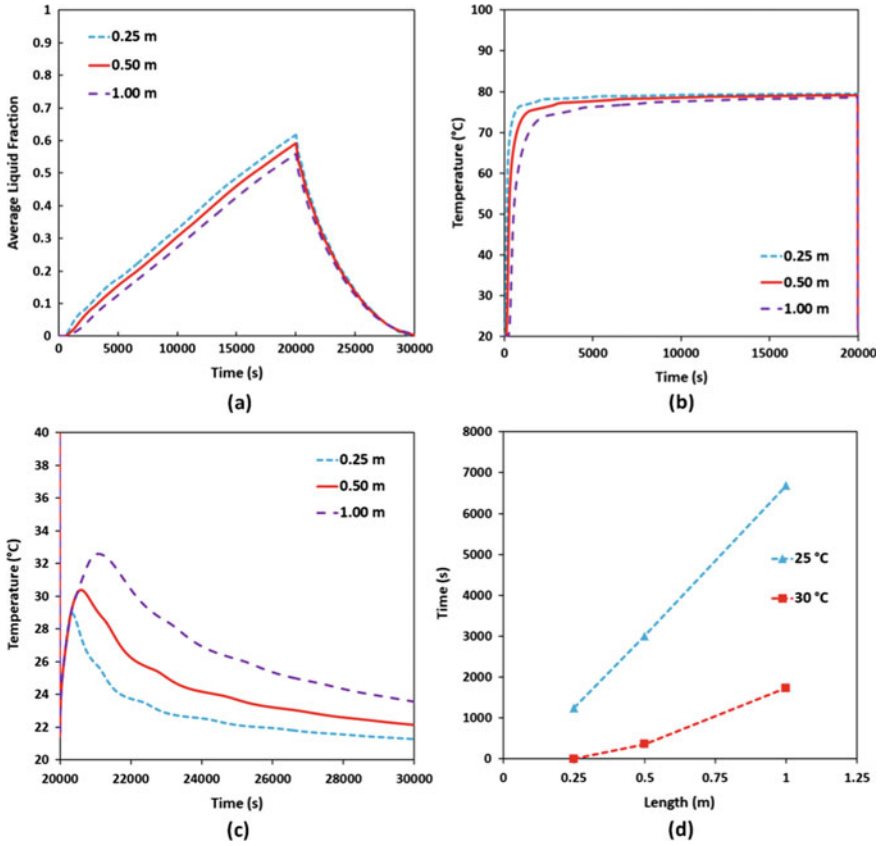


**Fig. 18** Variation of **a** liquid fraction with time, **b** water outlet temperature during charging, **c** water outlet temperature during discharging, and **d** time for obtaining water at specified temperature

charging for the three cases. It is seen that there is not much difference in temperature. The variation of liquid fraction is also similar. This is confirmed by the comparisons shown in Fig. 21a, b. However, the average outlet temperature is considerably different during the discharging process, as seen from Fig. 21c. Lower channel width results in faster heating of the water. This results in considerably longer duration at which water is obtained above prescribed thresholds of 25 °C and 30 °C (Fig. 21d).

## *6.7 Effect of Height of PCM Chamber*

The effect of PCM layer height is studied in this Sect. 3 and different PCM chambers are considered with PCM height of 0.02 m, 0.04 m, and 0.06 m. All the other parameters have the same value as given in Sect. 5.2. The variation of temperature and liquid

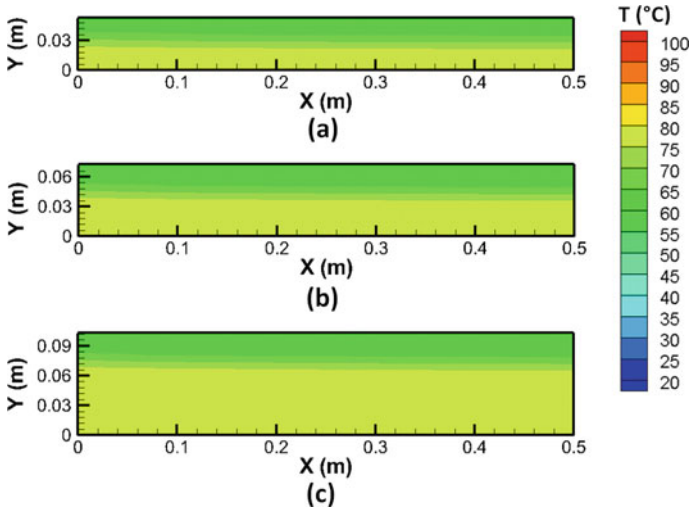


**Fig. 19** Temperature field at the end of charging cycle ($t$ = 20,000 s) with flow channel height equal to **a** 0.015 m, **b** 0.03 m, and **c** 0.06 m

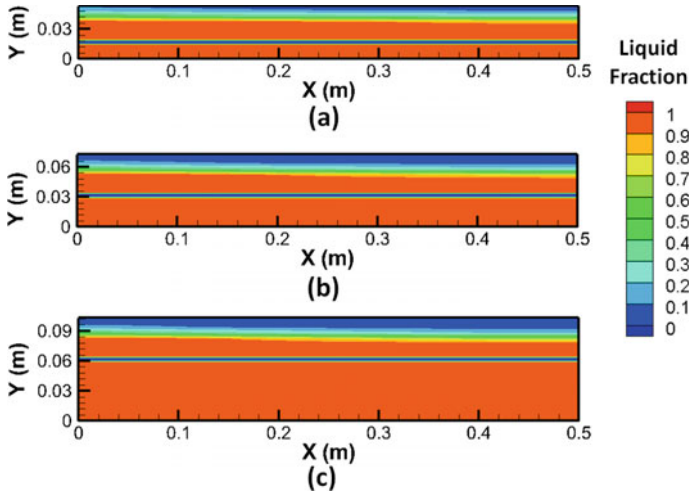


**Fig. 20** Liquid fraction at the end of charging cycle ($t$ = 20,000 s) with flow channel height equal to **a** 0.015 m, **b** 0.03 m, and **c** 0.06 m

fraction after the charging process for the three cases is compared in Figs. 22 and 23. It is seen that for lower height of PCM complete melting has occurred and subsequently sensible heating has raised the temperature of PCM significantly beyond the melting temperature. For the larger PCM domain, melting is partially complete and

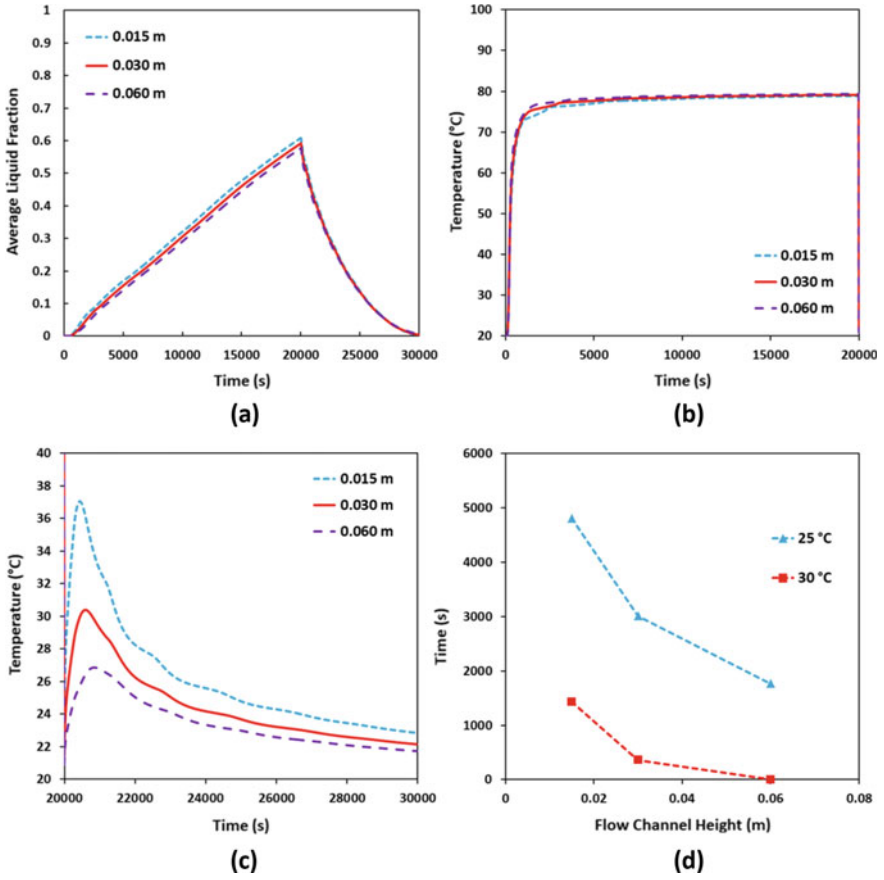


**Fig. 21** Variation of **a** liquid fraction with time, **b** water outlet temperature during charging, **c** water outlet temperature during discharging, and **d** time for obtaining water at specified temperature

the temperature is restricted to near melting temperature due to the phase change process.

The variation of liquid fraction with time for the three cases is compared in Fig. 24a. It is seen that the rate of increase of liquid fraction is considerably faster for the smaller PCM domain, and complete melting occurs after about 14,000 s. On the other hand, the maximum liquid fraction for the larger PCM domain is only about 30%. The water outlet temperatures are similar during charging (Fig. 24b) and discharging (Fig. 24c). The smaller PCM domain results in slightly higher water discharge temperature initially. Subsequently, the entire PCM solidifies and the outlet temperature drops below that for the other cases. Figure 24d shows that although the PCM domain height has significant influence on the discharge process, its effect is relatively less as compared to the effects of discharge flow velocity and domain length.

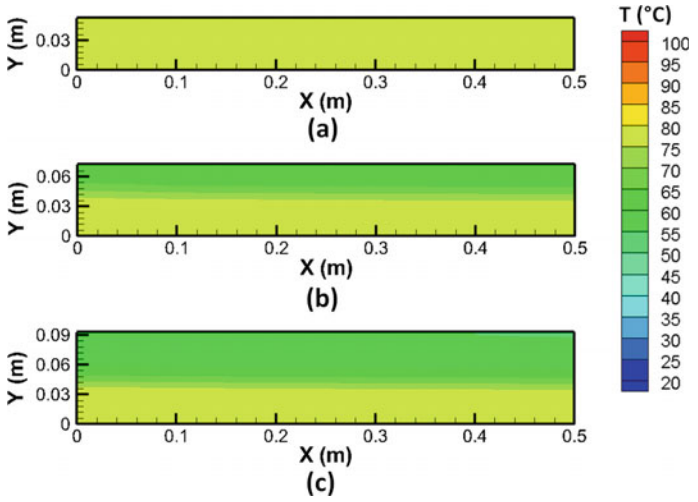


**Fig. 22** Temperature field at the end of charging cycle ($t$ = 20,000 s) with PCM height equal to **a** 0.02 m, **b** 0.04 m, **c** 0.06 m

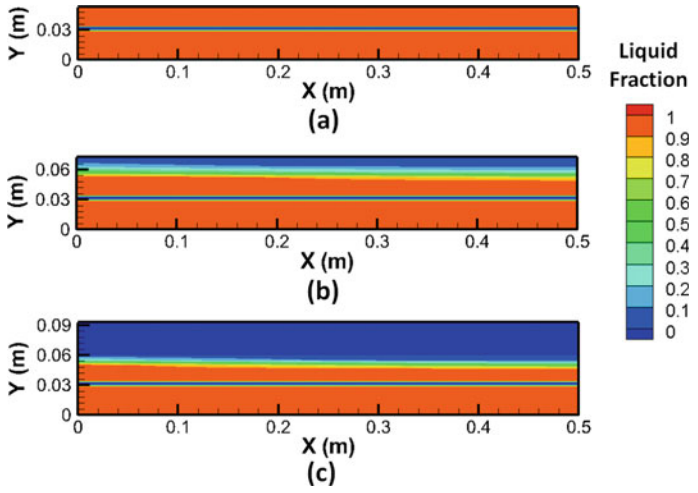


**Fig. 23** Liquid fraction at the end of charging cycle ($t$ = 20,000 s) with PCM height equal to **a** 0.02 m, **b** 0.04 m, **c** 0.06 m

## 7 Conclusion

An enthalpy-porosity-based model has been presented in this chapter for simulating the melting and solidification of PCM in a PCM-based solar water heater. The model captures the heat transfer to the PCM due to the flow of the heat transfer fluid. The effect of important flow parameters such as the flow inlet temperature and velocity

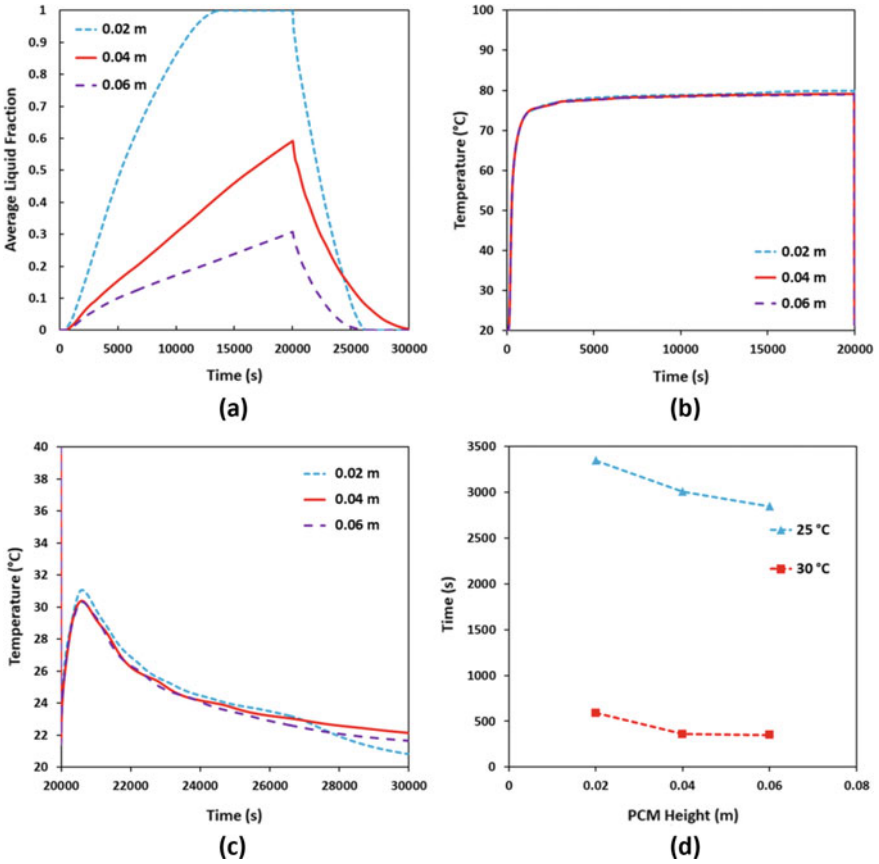


**Fig. 24** Variation of **a** liquid fraction with time, **b** water outlet temperature during charging, **c** water outlet temperature during discharging, and **d** time for obtaining water at specified temperature

and geometrical parameters such as the domain length, PCM chamber height and flow channel height on the melting pattern and discharge water temperature are analyzed. It is found that the discharge water temperature is strongly affected by the discharge flow velocity, and the length and height of the flow channel. The initial temperature of water during the charging cycle, the overall charging duration, and height of the PCM domain moderately affects the outlet water temperature during the discharging process. The effect of flow velocity during the charging process was found to be negligible. It can be inferred that to improve the performance of shell- and tube-type PCM-based solar water heaters, the geometrical parameters of the flow channel and the flow rate during the discharge process should be considered carefully.

## References

Abokersh MH, Osman M, El-Baz O, El-Morsi M, Sharaf O (2018) Review of the phase change material (PCM) usage for solar domestic water heating systems (SDWHS). Int J Energy Res 42(2):329–357

Adine HA, El Qarnia H (2009) Numerical analysis of the thermal behaviour of a shell-and-tube heat storage unit using phase change materials. Appl Math Model 33(4):2132–2144

Al-Hinti I, Al-Ghandoor A, Maaly A, Naqeera IA, Al-Khateeb Z, Al-Sheikh O (2010) Experimental investigation on the use of water-phase change material storage in conventional solar water heating systems. Energy Convers Manage 51(8):1735–1740

Alshaer WG, Nada SA, Rady MA, Le Bot C, Del Barrio EP (2015) Numerical investigations of using carbon foam/PCM/nano carbon tubes composites in thermal management of electronic equipment. Energy Convers Manage 89:873–884

Bansal NK, Buddhi D (1992) An analytical study of a latent heat storage system in a cylinder. Energy Convers Manage 33(4):235–242

Bouadila S, Fteïti M, Oueslati MM, Guizani A, Farhat A (2014) Enhancement of latent heat storage in a rectangular cavity: solar water heater case study. Energy Convers Manage 78:904–912

Cabeza LF, Mehling H, Hiebler S, Ziegler F (2002) Heat transfer enhancement in water when used as PCM in thermal energy storage. Appl Therm Eng 22(10):1141–1151

Chakraborty S, Dutta P (2001) A generalized formulation for evaluation of latent heat functions in enthalpy-based macroscopic models for convection-diffusion phase change processes. Metall Mater Trans 32(3):562

Dinesh BVS, Bhattacharya A (2019) Effect of foam geometry on heat absorption characteristics of PCM-metal foam composite thermal energy storage systems. Int J Heat Mass Transf 134:866–883

Dinesh BVS, Bhattacharya A (2020) Comparison of energy absorption characteristics of PCM-metal foam systems with different pore size distributions. J Energy Storage 28:101190

Fan L, Khodadadi JM (2012) A theoretical and experimental investigation of unidirectional freezing of nanoparticle-enhanced phase change materials. J Heat Transf 134(9):092301

Fazilati MA, Alemrajabi AA (2013) Phase change material for enhancing solar water heater, an experimental approach. Energy Convers Manage 71:138–145

Fukahori R, Nomura T, Zhu C, Sheng N, Okinaka N, Akiyama T (2016) Macro-encapsulation of metallic phase change material using cylindrical-type ceramic containers for high-temperature thermal energy storage. Appl Energy 170:324–328

Gharebaghi M, Sezai I (2007) Enhancement of heat transfer in latent heat storage modules with internal fins. Numer Heat Transf Part A Appl 53(7):749–765

Hawlader MNA, Uddin MS, Khin MM (2003) Microencapsulated PCM thermal-energy storage system. Appl Energy 74(1–2):195–202

Hosseini MJ, Ranjbar AA, Sedighi K, Rahimi M (2012) A combined experimental and computational study on the melting behavior of a medium temperature phase change storage material inside shell and tube heat exchanger. Int Commun Heat Mass Transf 39(9):1416–1424

Ismail KAR, Alves CLF, Modesto MS (2001) Numerical and experimental study on the solidification of PCM around a vertical axially finned isothermal cylinder. Appl Therm Eng 21(1):53–77

Joshi V, Rathod MK (2019) Thermal performance augmentation of metal foam infused phase change material using a partial filling strategy: an evaluation for fill height ratio and porosity. Appl Energy 253:113621

Kee SY, Munusamy Y, Ong KS (2018) Review of solar water heaters incorporating solid-liquid organic phase change materials as thermal storage. Appl Therm Eng 131:455–471

Kousksou T, Bruel P, Cherreau G, Leoussoff V, El Rhafiki T (2011) PCM storage for solar DHW: from an unfulfilled promise to a real benefit. Sol Energy 85(9):2033–2040

Mahfuz MH, Anisur MR, Kibria MA, Saidur R, Metselaar IHSC (2014) Performance investigation of thermal energy storage system with Phase Change Material (PCM) for solar water heating application. Int Commun Heat Mass Transf 57:132–139

Mat S, Al-Abidi AA, Sopian K, Sulaiman MY, Mohammad AT (2013) Enhance heat transfer for PCM melting in triplex tube with internal–external fins. Energy Convers Manage 74:223–236
Mehling H, Cabeza LF, Hippeli S, Hiebler S (2003) PCM-module to improve hot water heat stores with stratification. Renew Energy 28(5):699–711
Meng ZN, Zhang P (2017) Experimental and numerical investigation of a tube-in-tank latent thermal energy storage unit using composite PCM. Appl Energy 190:524–539
Morales-Ruiz S, Rigola J, Oliet C, Oliva A (2016) Analysis and design of a drain water heat recovery storage unit based on PCM plates. Appl Energy 179:1006–1019
Nagano K, Ogawa K, Mochida T, Hayashi K, Ogoshi H (2004) Performance of heat charge/discharge of magnesium nitrate hexahydrate and magnesium chloride hexahydrate mixture to a single vertical tube for a latent heat storage system. Appl Therm Eng 24(2–3):209–220
Nallusamy N, Sampath S, Velraj R (2007) Experimental investigation on a combined sensible and latent heat storage system integrated with constant/varying (solar) heat sources. Renew Energy 32(7):1206–1227
Nayak KC, Saha SK, Srinivasan K, Dutta P (2006) A numerical model for heat sinks with phase change materials and thermal conductivity enhancers. Int J Heat Mass Transf 49(11–12):1833–1844
Oró E, De Gracia A, Castell A, Farid MM, Cabeza LF (2012) Review on phase change materials (PCMs) for cold thermal energy storage applications. Appl Energy 99:513–533
Patankar S (2018) Numerical heat transfer and fluid flow. CRC Press, Boca Raton
Prakash J, Garg HP, Datta G (1985) A solar water heater with a built-in latent heat storage. Energy Convers Manage 25(1):51–56
Reddy RM, Nallusamy N, Reddy KH (2012) Experimental studies on phase change material-based thermal energy storage system for solar water heating applications. J Fundam Renew Energy Appl 2
Sahoo SK, Rath P, Das MK (2016) Numerical study of phase change material based orthotropic heat sink for thermal management of electronics components. Int J Heat Mass Transf 103:855–867
Sahoo SK, Rath P, Das MK (2019) Solidification of phase change material nanocomposite inside a finned heat sink: a macro scale model of nanoparticles distribution. J Therm Sci Eng Appl 11(4):041005
Seddegh S, Wang X, Henderson AD, Xing Z (2015) Solar domestic hot water systems using latent heat energy storage medium: a review. Renew Sustain Energy Rev 49:517–533
Shaikh S, Lafdi K, Hallinan K (2008) Carbon nanoadditives to enhance latent energy storage of phase change materials. J Appl Phys 103(9):094302
Shrivastava A, Chakraborty PR (2019) Shell-and-tube latent heat thermal energy storage (ST-LHTES). In: Advances in solar energy research. Springer, Singapore, pp 395–441
Voller VR, Brent AD, Prakash C (1989) The modelling of heat, mass and solute transport in solidification systems. Int J Heat Mass Transf 32(9):1719–1731
Zhang Y, Faghri A (1996) Heat transfer enhancement in latent heat thermal energy storage system by using the internally finned tube. Int J Heat Mass Transf 39(15):3165–3173
Zhou D, Zhao CY (2011) Experimental investigations on heat transfer in phase change materials (PCMs) embedded in porous materials. Appl Therm Eng 31(5):970–977